Journal of Power Sources 237 (2013) 112–118

Contents lists available at SciVerse ScienceDirect

Journal of Power Sources

journal homepage: www.elsevier.com/locate/jpowsour

Novel ε-$Cu_{0.95}V_2O_5$ hollow microspheres and α-CuV_2O_6 nanograins: Facile synthesis and application in lithium-ion batteries

Wen Hu [a,b], Xinchuan Du [b], Yaoming Wu [b], Limin Wang [b,*]

[a] Faculty of Materials Science and Engineering, Kunming University of Science and Technology, Kunming 650093, Yunnan, China
[b] State Key Laboratory of Rare Earth Resource Utilization, Changchun Institute of Applied Chemistry, Chinese Academy of Sciences, Changchun 130022, Jilin, China

HIGHLIGHTS

- Self-assembled micro-nano ε-$Cu_{0.95}V_2O_5$ is easily fabricated by solution method.
- ε-$Cu_{0.95}V_2O_5$ superstructures reversibly react with 2.75 Li.
- Copper immobilization is highly desired indicated by *ex situ* XRD investigations.
- Calcinating the prepared ε-$Cu_{0.95}V_2O_5$ forms single-crystalline α-CuV_2O_6 nanograins.
- The calcined α-CuV_2O_6 shows broad prospects in long-term and high-rate primary LBs.

GRAPHICAL ABSTRACT

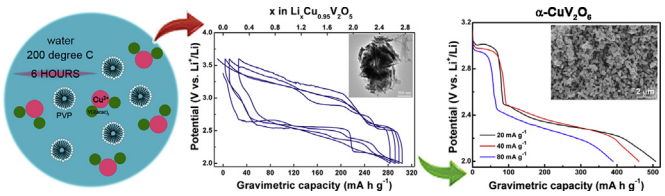

ARTICLE INFO

Article history:
Received 15 October 2012
Received in revised form
26 February 2013
Accepted 2 March 2013
Available online 14 March 2013

Keywords:
Copper dissolution
Lithium batteries
Nanostructures
Self-assembly
Vanadate

ABSTRACT

Novel ε-$Cu_{0.95}V_2O_5$ hollow microspheres assembled by single-crystalline nanoribbons can be easily synthesized directly from a hydrothermal reaction between V(IV)O(acac)$_2$ and $Cu(NO_3)_2$ in a solution containing a proper amount of polymer polyvinyl pyrrolidone (PVP, K30). A possible growth mechanism has been proposed. Electrochemical measurements demonstrate that the as-prepared ε-$Cu_{0.95}V_2O_5$ superstructures display a reversible capacity of 304 mAh g^{-1}, and could sustain respectable rate capability. By reinvestigating the cooperative displacement/intercalation (CDI) mechanism of ε-$Cu_{0.95}V_2O_5$ using cyclic voltammetry (CV), *ex situ* XRD, and *ex situ* SEM–EDS techniques, it is found that the copper dissolution problem, which leads to poor capacity retention of cells operating on Li-driven Cu extrusion –insertion process, has not been well tackled due to its superstructure collapse. Rational electrode configuration design is urgently needed. In addition, single-crystalline α-CuV_2O_6 nanograins are obtained by calcining the micro-nanostructured ε-$Cu_{0.95}V_2O_5$ precursor. The post-treated α-CuV_2O_6 exhibits high discharge capacity of 507 mAh g^{-1} at 20 mA g^{-1} and 390 mAh g^{-1} at 80 mA g^{-1}, indicating it is a promising cathode candidate for long-term and high-rate lithium primary batteries.

© 2013 Elsevier B.V. All rights reserved.

1. Introduction

The increasing demand for electricity storage in energy-harvesting landscape such as electrical vehicles and renewable stationary energy has been promoting intensive research efforts on high capacity lithium ion batteries (LIBs). However, the performance offered by today's insertion compounds has already reached their peak dictated by the 1e$^-$/formula electrochemistry. To achieve impressive capacity gains, exploring advanced materials enabling reversible multi-electron charge transfer is highly desired. Some new reaction mechanisms have been proposed recently [1–9], for example, the Li electrochemically driven MO_x (or nitrides and fluorides) → M (M = Fe, Co, etc.) conversion process [1–3];

* Corresponding author. Tel./fax: +86 431 85262447.
E-mail address: lmwang@ciac.jl.cn (L. Wang).

0378-7753/$ – see front matter © 2013 Elsevier B.V. All rights reserved.
http://dx.doi.org/10.1016/j.jpowsour.2013.03.002

successive structural phase transformations occurring upon lithium intercalation via vanadium oxide composites [4]; the cooperative displacement/intercalation (CDI) mechanism for coinage elements (Cu, Ag and Ni)-based thiospinels, chevrel phase and $Cu_{2.33}V_4O_{11}$ in LIBs [5–7]; Si, O_2 and S operate through combination reaction involving Li–Si alloys, lithium oxides and chalcogenides formation [8,9]. Unfortunately, their interests as bulk electrode materials are limited by the low electronic conductivity and significant capacity fading during cycling. Reducing particle's size to nanoscale dimensions or introduction of hierarchical mixed-conducting networks would make the electroactivity dominated by interface chemistry with consequences such as defects or band bending. This leads to a significant alteration of the electrochemical properties with respect to well-established bulk phenomena. Nanostructuring has been becoming very helpful in improving the electroactivity (e.g. Li storage in nanosized Fe_2O_3) and life span of electrode materials (e.g. Li storage in nanostructured Si and nanocomposite C–S) [10–12].

Layered ε-$Cu_{0.95}V_2O_5$ bronze possesses metallic conductivity, and exhibits a partial reversible copper displacement reaction that when combined with the vanadium redox couple affords a gravimetric capacity of 290 mAh g^{-1} at 2.0 V reported in the literature [13–17]. The good conductivity and high energy density showed by ε-copper vanadium bronze has led to its exploration as promising cathode candidate for LIBs. However, to the best of our knowledge, almost all previous works use ceramic approach to prepare bulk ε-phase sample:

$$Cu + V_2O_5 \xrightarrow[\text{Vac. or } N_2 \text{ flow}]{630\ ^\circ C} \varepsilon\text{-}CuV_2O_5 \quad (1)$$

wherein the experimental conditions are rigorous (e.g. nonoxidizing atmosphere is a must to avoid formation of CuV_2O_6), and the operating procedures are complicated (e.g. grinding raw material powers sufficiently → pelletization → heat treatment → pulverization → repeat above procedures twice). And as noted above, in bulk ε-$Cu_{0.95}V_2O_5$ the CDI process is partial reversible, thus presents unsatisfied cycling behavior. Encouragingly, the irreversibility problem also encountered by bulk V_2O_5, $Ag_2V_4O_{11}$, etc. has recently been tackled by nanostructuring strategy [18–20]. Combined with the greater conductivity of ε-$Cu_{0.95}V_2O_5$ than V_2O_5 and $Ag_2V_4O_{11}$, nanostructured ε-copper vanadium bronze may potentially show improved Li-ion/Cu-ion exchange kinetics, Li-ion insertion/extraction kinetics and cycling stability because of improved solid state diffusion kinetics, better interfacial contact with the electrolyte, and the operation of Li-ion storage mechanisms not accessible for bulk counterparts.

Herein, we put forward a facile soft chemistry method to self-assemble ε-$Cu_{0.95}V_2O_5$ nanoribbons into hollow microspheres. A redox hydrothermal route is adopted, in which $Cu(NO_3)_2\cdot 3H_2O$ (as an oxidant) reacts with stoichiometric vanadium(IV)-oxy acetylacetonate ($V(IV)O(acac)_2$, as a reductant) in the presence of poly(-vinylpyrrolidone) (PVP, as a capping reagent). It is worth noting that the two metal-ion precursors with right-valences simultaneously can act as redox sources, which avoid the use of foreign reductant [21–25], hence the preparation procedure is greatly simplified and the risk of introduced impurity in the final product is eliminated. The overall chemical reaction can be briefly described in equation (2). Electrochemical investigations reveal that the prepared ε-$Cu_{0.95}V_2O_5$ is electroactive with high capacity and desirable rate capability, whereas reversibility improvement responds spherical mirco-nanoarchitecture to little effect.

$$Cu^{2+} + 2V(IV)O(acac)_2 + 3H_2O \rightarrow \varepsilon\text{-}CuV_2O_5 + 4Hacac + 2H^+ \quad (2)$$

In practical application like implantable cardioverter defibrillator, primary lithium batteries are also facing more stringent challenges, including larger discharge capacity and higher power capability. Since the performance is mainly cathode limited, seeking $Ag_2V_4O_{11}$ alternative advanced materials is of great scientific and technological importance [26–28]. Copper vanadate CuV_2O_6 is of particular interest. In this work, the as-synthesized ε-$Cu_{0.95}V_2O_5$ hollow microspheres can be calcined into single-crystalline α-CuV_2O_6 nanograins. This material delivers a large discharge capacity of 507 mAh g^{-1} at 20 mA g^{-1} (above 2.0 V) and excellent rate capability, thus becomes a promising candidate for long-term primary lithium batteries.

2. Experimental

Cupric nitrate trihydrate ($Cu(NO_3)_2\cdot 3H_2O$, Beijing chemical works, AR), cupric chloride dihydrate ($CuCl_2\cdot 2H_2O$, Beijing chemical works, AR), cupric sulfate pentahydrate ($CuSO_4\cdot 5H_2O$, Beijing chemical works, AR), cupric acetate monohydrate ($Cu(CH_3COO)_2\cdot H_2O$, Beijing chemical works, AR), cupric acetylacetonate ($Cu(acac)_2$, Aladdin reagent, AR), vanadium(IV)-oxy acetylacetonate ($V(IV)O(acac)_2$, Aladdin reagent, AR), poly(vinylpyrrolidone) (PVP, K30, Tianjin TianTai Fine Chemical Co, Ltd., AR), deionized water, absolute alcohol and acetylene black (Hong-xin chemical works), N-methyl-2-pyrrolidinone (NMP, Aladdin reagent, AR), PVDF (Dupont company, 99.9%), separator (polypropylene film, Celgard), electrolyte (1 M $LiPF_6$ in ethylene carbonate (EC)/dimethyl carbonate (DMC) with the weight ratio of 1:1, Zhangjiagang guotai-huarong new chemical materials Co., Ltd). All the chemicals were used as received.

$V(IV)O(acac)_2$ (0.024 mmol, 0.0636 g) was added into the PVP (0.15 g L^{-1}, 24 mL) solution to form homogeneous solution after magnetic stirring (ultrasonic irradiation) for 15 min. Then stoichiometric amount of $Cu(NO_3)_2\cdot 3H_2O$ (0.012 mmol, 0.029 g) was dispersed into the 24 mL $V(IV)O(acac)_2$/PVP/deionized water blending. After the mixture had been stirred and then ultrasonication for 10 min, the resulting precursor solution was transferred into 30 mL Teflon-linked stainless steel autoclave. The autoclave was heated to 200 °C at the heating rate of 5 °C min^{-1} and maintained at 200 °C for 6 h, then cooled to room temperature naturally. The obtained black solids were collected by centrifugation, washed by deionized water and ethanol, and then vacuum dried at 70 °C for 12 h.

To investigate the phase structures of the products, X-ray diffraction (XRD) patterns were recorded by a Bruker D8 Focus power X-ray diffractometer with Cu Kα radiation. The chemical composition of the sample was determined by POEMS ICP–MS. Scanning electron microscope (SEM) was performed by a Hitachi S-4800 field emission scanning electron microscope, whereas the energy dispersive X-ray spectroscopy (EDS) was done using a Bruker AXS microanalysis at an accelerating voltage of 20 kV. Samples for SEM were prepared by dispersing the as-prepared product in ethanol by sonicating for about 30 min, and then depositing the sample onto a silicon wafer, attached to a SEM brass stub. A Philips TF-F20 (200 kV) transmission electron microscope (TEM) with an energy-dispersive X-ray spectrometer was used to obtain SAED patterns and local compositional information and to study the phase microstructure. Samples for all of these TEM experiments were prepared by dispersing the samples in ethanol, sonicating for 30 min to ensure adequate dispersion of the nanostructures, and evaporating one drop of the solution onto a 300 mesh Cu grid, coated with a lacey carbon film. The oxidation states of the constituent elements were measured with X-ray photoelectron spectroscopy (XPS) using Thermo ESCALAB 250 system and the XPSPEAK software was used for the fitting of the XPS spectra.

The positive electrodes were fabricated by mixing 80 wt% active materials, 10 wt% acetylene black and 10 wt% PVDF binder in appropriate amount of NMP as solvent. Then the resulting paste was spread on an aluminum foil by automatic film coater (micrometer doctor blade, MTI). After the NMP solvent evaporation in a vacuum oven at 120 °C for 12 h, the electrodes were pressed and cut into disks. A CR2032 coin-type cell was assembled with lithium metal as the counter and reference electrode and polypropylene film as a separator. The cells were constructed and handled in an argon-filled glove box. The charge–discharge measurements were carried out using the Land battery system (CT2001A) at a constant current density in a voltage range of 2–3.6 V versus Li/Li^+. The cells discharged/charged to different voltages and maintained at that voltage for 3 h were opened in the glove box, and the positive electrodes were washed with DMC and dried in the vacuum oven at 90 °C for 12 h. Then the working electrodes were analyzed by XRD.

3. Results and discussion

Fig. 1a shows the XRD pattern of the hydrothermal product obtained with 0.15 g L^{-1} PVP and dwell time of 6 h. All the diffraction peaks can be indexed to the monoclinic ε-copper vanadium bronze (space group C2/m, PDF #18-0463). A visualization of the crystal structure depicting the ε-$Cu_{0.85-1}V_2O_5$ unit cell is shown in Figure S1. Fig. 1b shows the typical SEM image displaying large quantity of uniform microspheres with 1.5–3 μm in diameter. The detailed morphology of the microspherical architecture (inset in Fig. 1b) reveals that the short nanoribbon units connect to each other through the center and circle around to form the spherical shell just taking the shape of a flower. A broken sphere in the middle part of Fig. 1b clearly shows the hollow feature of the sphere. The energy dispersive X-ray spectroscopy (EDS) pattern (Figure S2) shows that the atomic ratio of Cu to V in the sample is 0.46, approaching the chemical composition result measured by inductively coupled plasma mass spectrometry (ICP–MS), namely copper and vanadium occupy 240.6 mg g^{-1} and 380.5 mg g^{-1}, respectively. Therefore, the formula of the sample is determined as ε-$Cu_{0.95}V_2O_5$. The TEM image in Fig. 1c confirms the hollow microsphere superstructure of the ε-phase with nanoribbons pointing out from the surface. The microstructure of the product is further studied by means of selected-area electron diffraction (SAED) and high-resolution transmission electron microscopy (HRTEM). Taken from the edge of a nanoribbon (Fig. 1d), the SAED pattern along [010] zone axis orientation is obtained (upper inset in Fig. 1d). It should be noted that in this [010] SAED pattern a regular appearance of some forbidden spots (marked with small pink circles) is observed besides the allowed diffraction spots. As elucidated before [22,29–31], we figure that this phenomenon results from Cu(2) ordering, meaning a superlattice structure with c-doubling appear. In the representative HRTEM image (lower inset in Fig. 1d), the lattice fringes are clearly visible with a spacing of 0.355 nm, which is in good agreement with the spacing of the (110) planes of ε-$Cu_{0.95}V_2O_5$. High-resolution photoelectron spectroscopy (XPS) spectra (Figure S3) reveal that V is mixed-valent between V^{3+}, V^{4+} and V^{5+}, and that the major copper species is Cu^+ together with a small amount of Cu^{2+}. Part of the Cu^{2+} signal likely originates from the residue $Cu(NO_3)_2$ precursor and surface oxidation. But it is also possible for Cu^{2+} to occupy some of the interstitial sites within the ε-$Cu_{0.95}V_2O_5$ bronze considering the multiplication of Cu sites and various coordination numbers for Cu element. Actually, Savariault [21], Banerjee [32] et al. have noted the occupation of tunnel sites by both Cu^+ and Cu^{2+} in micrometer-sized β′-$Cu_xV_2O_5$ ($0.26 \leq x \leq 0.67$). The formation of Cu^+ and V^{5+} well illustrates the feasibility of our design about direct redox reaction between Cu^{2+}

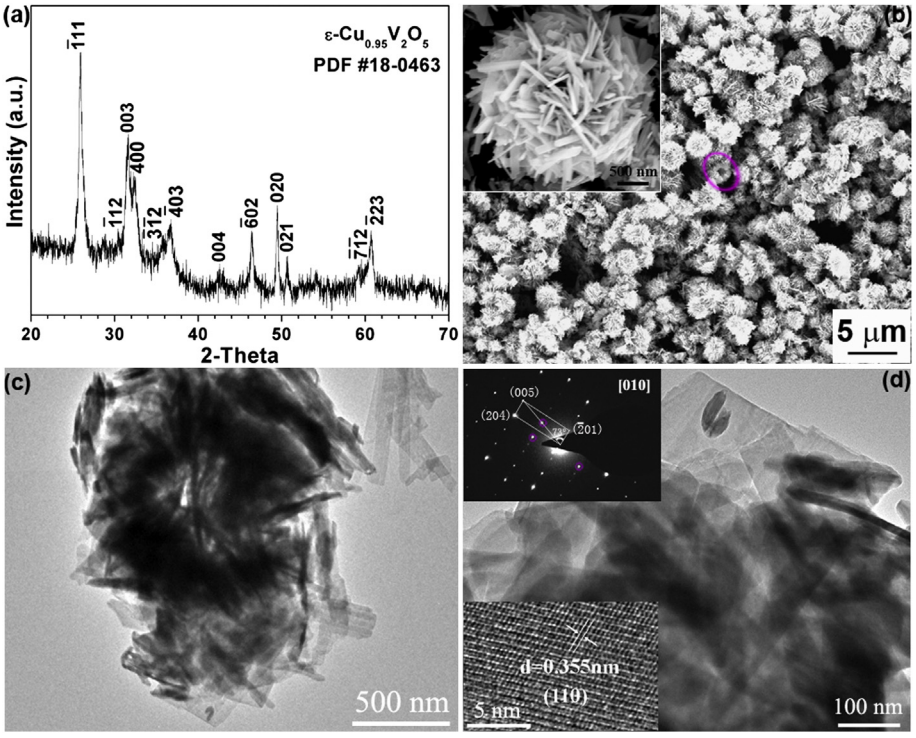

Fig. 1. (a) XRD, (b) SEM, and (c, d) TEM images of the as-prepared flowerlike ε-$Cu_{0.95}V_2O_5$ hollow microspheres obtained in the presence of stoichiometric amount of $Cu(NO_3)_2$ and $VO(acac)_2$ and 0.15 g L^{-1} PVP at 200 °C. A broken microsphere marked by a pink circle in (b) is indicative of their hollow feature. The inset in (b) is the detailed SEM view of an individual hollow microsphere with nanoribbons circle around. (d) TEM image of ε-$Cu_{0.95}V_2O_5$ fragment. The top inset in (d) is the [010] zone SAED pattern, and the bottom inset is the HRTEM lattice image. (For interpretation of the references to colour in this figure legend, the reader is referred to the web version of this article.)

and V^{4+} precursors, while the appearance of V^{3+} may arise from the V^{4+} disproportionation reaction.

In order to gain insight into the formation mechanism of the flowerlike ε-$Cu_{0.95}V_2O_5$ micro-nanostructures, products collected at different growth stages are subjected to XRD and SEM investigations. From the XRD patterns shown in Figure S4, the hydrolyzation of $VO(acac)_2$ (equation (3)) is the rate-determining step. In Figure S5 SEM images indicate that the microspherical geometry can be readily shaped very soon after hydrothermal reaction starts. Besides the reaction time, polymer PVP is also an important controlling factor (Figure S6). Only when PVP concentration is approximately 0.15 g L^{-1}, monodispersive ε-$Cu_{0.95}V_2O_5$ microspheres can be formed. Otherwise, PVP spherical micelles cannot be formed, thus only primary ε-$Cu_{0.95}V_2O_5$ nanoribbons are obtained (PVP concentration $\ll$ 0.15 g L^{-1}), or the developing ε-$Cu_{0.95}V_2O_5$ microspheres pack tightly and finally coagulate (PVP concentration $\gg$ 0.15 g L^{-1}). In addition, XRD patterns of the as-prepared ε-$Cu_{0.95}V_2O_5$ samples with different PVP dosage shown in Figure S7 imply that the adsorption of PVP act as a selective crystal face inhibitor to inhibit the faster growth along the [001] direction. The similar crystal growth modifying effect of PVP has ever been established in the formation of inorganic ordered superstructures [33,34]. Moreover interestingly, diverse hierarchy ε-$Cu_{0.95}V_2O_5$ assemblies are observed when various cupric salt with different ionicity is used in hydrothermal system. See details in Figure S8.

$$V(IV)O(acac)_2 + 5H_2O + 2H^+ \rightleftharpoons [V(IV)O(H_2O)_5]^{2+} + 2Hacac \quad (3)$$

Thereafter, a possible mechanism for the evolution of uniform ε-$Cu_{0.95}V_2O_5$ hollow microspherical structures is proposed (Fig. 2). Provided with the optimized hydrothermal conditions, PVP begins to form spherical micelles as soon as accomplishing batch feeding. The reaction starts from the slow hydrolyzation of $VO(acac)_2$ to $[VO(H_2O)_5]^{2+}$, which are quickly adsorbed on the outside hydrophilic carbonyl groups of PVP micelles. Then Cu^{2+} induces $[VO(H_2O)_5]^{2+}$ to condense exclusively in an edge sharing manner to form layer structure of the final ε-$Cu_{0.95}V_2O_5$. Subsequently, Cu^{2+} inserts into V_2O_5 framework of $[VO(H_2O)_5]^{2+}$ and attacks toward V^{4+} centers to carry through their redox reaction. Once the reaction is accomplished, primary ε-$Cu_{0.95}V_2O_5$ nuclei are formed. The obtained ε-$Cu_{0.95}V_2O_5$ nuclei aggregate and grow into nanoribbons according to the well-known Ostwald ripening mechanism. After 6 h, the ripening ε-$Cu_{0.95}V_2O_5$ microspheres with nanoribbon building blocks are finely evolved. Hollow spheres retain their geometry even after PVP is removed.

The cathode performance of the highly ordered ε-$Cu_{0.95}V_2O_5$ superstructures has been tested with respect to lithium metal. Fig. 3a is the typical galvanostatic profile in the potential range of 2–3.6 V at 20 mA g^{-1}. The first discharge capacity is 304 mAh g^{-1} (2.75 Li^+ uptake), and upon recharge most of the reacted lithium can be removed. Even at a high current density of 300 mA g^{-1}, this material can still deliver 190 mAh g^{-1} capacity (Figure S9). The large reversible capacity and respectable rate capability suggest the high electroactivity of hollow micro–nano ε-$Cu_{0.95}V_2O_5$. Multiple voltage plateaus in the first discharge and charge curves can be better illustrated using cyclic voltammetry (CV) shown in Fig. 3b. Four sets of reduction peaks can be seen at 3.32, 2.65, 2.51, and 2.14 V. To obtain deep insight into the lithiation–delithiation mechanism in ε-$Cu_{0.95}V_2O_5$ hollow microspheres, we performed *ex situ* XRD study of electrodes recovered from multiple cells discharged or charged to selected voltage. From Fig. 3c, these cathodic peaks have been attributed to four successive electrochemical processes (equations (4)–(7)).

$$\varepsilon\text{-}Cu_{0.95}V_2O_5 + x\left(Li^+ + e^-\right) \rightarrow \varepsilon\text{-}Li_xCu_{0.95}V_2O_5 \quad (0 \le x \le 0.2) \quad (4)$$

$$\varepsilon\text{-}Li_{0.2}Cu_{0.95}V_2O_5 + x'\left(Li^+ + e^-\right) \rightarrow \varepsilon\text{-}Li_{0.2+x'}Cu_{0.95-x'}V_2O_5 + x'Cu \quad (0 \le x' \le 0.95) \quad (5)$$

$$\varepsilon\text{-}Li_{1.15}V_2O_5 + x''\left(Li^+ + e^-\right) \rightarrow \delta\text{-}Li_{1.15+x''}V_2O_5 \quad (0 \le x'' \le 0.85) \quad (6)$$

$$\delta\text{-}Li_{2.0}V_2O_5 + x'''\left(Li^+ + e^-\right) \rightarrow \gamma\text{-}Li_{2.0+x'''}V_2O_5 \quad \left(0 \le x''' \le 0.75\right) \quad (7)$$

From Fig. 3b, the reverse reactions take place as indicated by the four oxidation peaks located at 2.52, 2.72, 2.92, and 3.15 V. Among them, however, the anodic peak appeared at 2.72 V is so weak that the *ex situ* XRD pattern recorded at 2.83 V does not detect any phase transition information compared with that of 2.60 V (Fig. 3c). Lithium delithiation is summarized by equations (8)–(10). Since α-, ε-, δ-, γ-, and ω-$Li_xV_2O_5$, well known successively formed in the electrochemical reaction of Li insertion into V_2O_5 at room

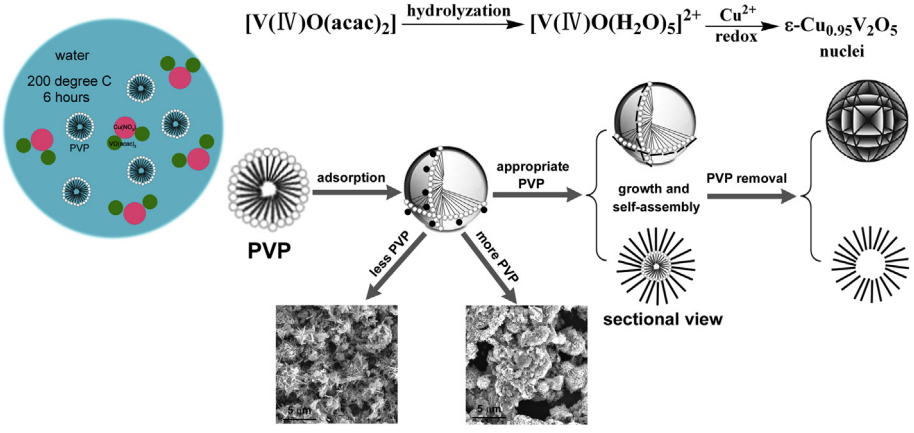

Fig. 2. Evolution mechanism of ε-$Cu_{0.95}V_2O_5$ hollow microspheres.

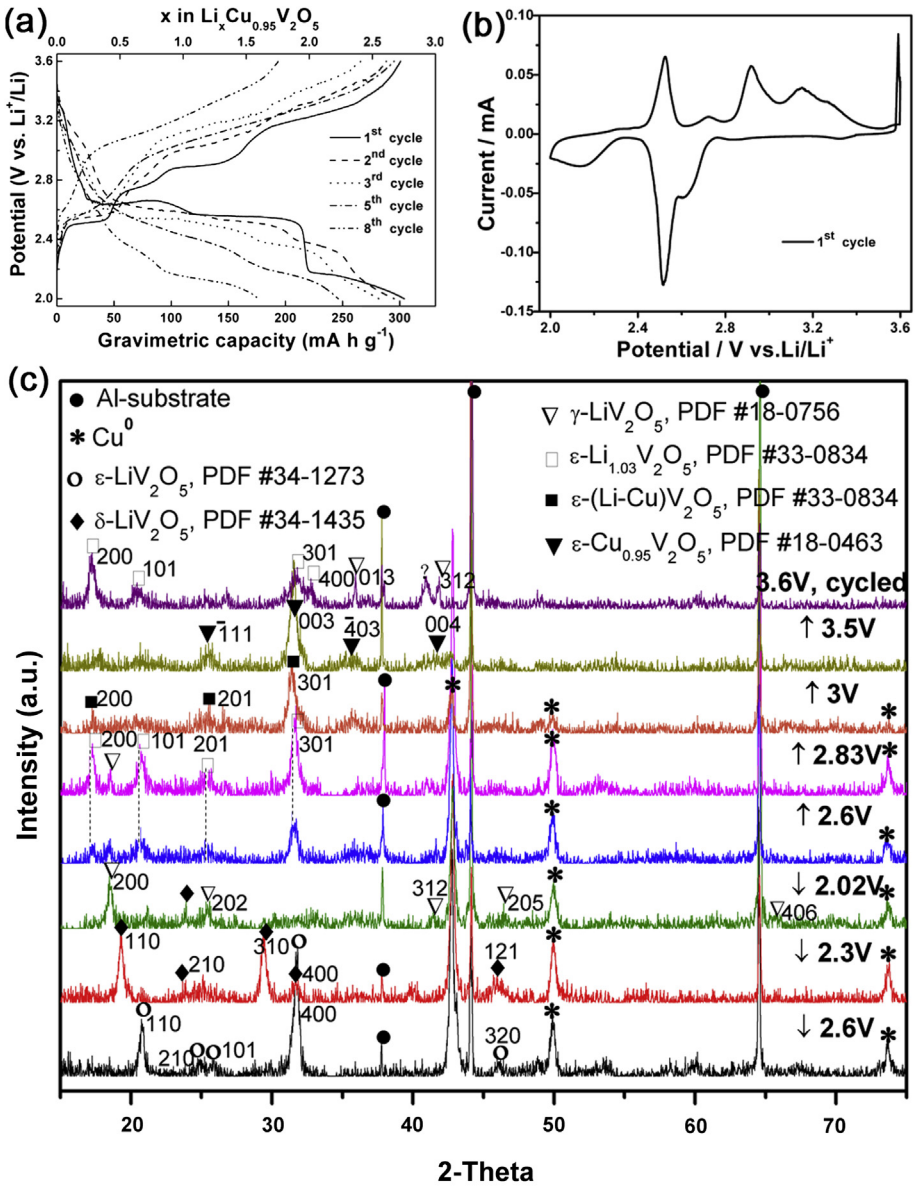

Fig. 3. (a) Room-temperature potential composition–capacity profile for a ε-$Cu_{0.95}V_2O_5$/Li cell cycled in the 2–3.6 V voltage window at 20 mA g^{-1}. (b) CV curve in the first cycle at a scan rate of 0.01 mV s^{-1} in the voltage range of 2–3.6 V. (c) *Ex situ* XRD patterns of ε-$Cu_{0.95}V_2O_5$ electrodes discharged (↓) or charged (↑) to different depths of voltage and charged to 3.6 V after 8 cycles.

temperature, exist within the Li content range being $x < 0.01$, $0.35 < x < 0.7$, $0.9 < x \leq 1$, $1 < x \leq 2$, and $2 < x \leq 3$ respectively [35], it is necessary here for us to make explanations on the over-lithiated ε (x up to 1.85)-, δ (x up to 2)-, and γ (x up to 2.75)-$Li_xV_2O_5$ proposed in the lithiation/delithiation mechanism of ε-$Cu_{0.95}V_2O_5$ cathode with lithium. Reasons are as follows. Firstly, considering the fact that over-lithiated ε (x up to 2.75)-$Li_xV_2O_5$ phase has already been identified in the electrochemical reaction between δ-$Ag_{0.75}V_2O_5$ and Li at room temperature [36], it seems that metal vanadium bronzes can tolerate over-lithiation owing to their more rigid host lattices than V_2O_5. Secondly, in spite of 2.75 Li^+ uptake by ε-$Cu_{0.95}V_2O_5$, ω-$Li_3V_2O_5$ formation is impossible. Because as mentioned in the literature [35], the rock salt type structure of ω phase differs completely from that of all other materials involved in the various $Li_xV_2O_5$ systems, meaning that if deep discharge of a Li||ε-$Cu_{0.95}V_2O_5$ battery ($x > 2$) forms ω-$Li_3V_2O_5$, the primary ε framework could not be recovered after the following recharge process, which is obviously inconsistent with our experimental fact. Then combined with the *ex situ* XRD result, we inferred that further lithiation of ε-$Li_{1.15}V_2O_5$ would lead to successive over-lithiated δ ($x > 1$, equation (6)) and γ ($x > 2$, equation (7)) phases formation, and vice versa for the following delithiation. Anyway the recrystallization of ε-copper vanadate structure infers that the overall electrochemical behavior is reversible, and that a delicate balance exists between three underlying processes, i.e. ion diffusion (Cu-out/Li-in and *vice versa*), V reduction/oxidation, and rearrangement of the initial electrode material.

$$\gamma\text{-}Li_{2.75}V_2O_5 \rightarrow \varepsilon\text{-}Li_{2.75-y}V_2O_5 + y\left(Li^+ + e^-\right) \quad (0 \leq y \leq 0.9) \tag{8}$$

$$\varepsilon\text{-}Li_{1.85}V_2O_5 + y'Cu \rightarrow \varepsilon\text{-}Li_{1.85-y'}Cu_{y'}V_2O_5 + y'\left(Li^+ + e^-\right) \quad (0 \leq y' \leq 0.77) \tag{9}$$

$$\varepsilon\text{-}Li_{1.08}Cu_{0.77}V_2O_5 \rightarrow \varepsilon\text{-}Li_{1.08-y''}Cu_{0.77}V_2O_5 + y''\left(Li^+ + e^-\right) \quad (0 \le y'' \le 1.05) \tag{10}$$

But on the other hand, from equation (9) one can also see the copper dissolution issue, which arises from the competing rate of copper-ions reinjection into ε Li–V–O matrix versus copper-ions migration to the anodic side. After eight cycles of discharge and charge, Cu element signal can no longer be detected in the positive electrode (Figure S10b). Copper-ions escape is not just a matter of active material loss for the cathode, but can lead to more serious complications, for instance, the electronic conductivity of ε-vanadium bronze is getting worse, and the lithium negative electrode surface is progressively poisoned by the presence of metallic Cu. Owing to these intrinsic drawbacks, the capacity retention of ε-$Cu_{0.95}V_2O_5$ cathode is poor (Fig. 3a). In fact, our original intention is to expect the hollow microspheres together with the 1D nanoribbons would be favorable in improving the Li-ion/Cu-ion exchange efficiency, and alleviating Cu-ions dissolution to some extent [37–39]. Unfortunately, SEM image (Figure S10a) shows the breakdown of ε-$Cu_{0.95}V_2O_5$ superstructure after the 1st cycle. We are presently studying various possibilities, by acting on either the electrode configuration (e.g. ε-$Cu_{0.95}V_2O_5$ hollow microspheres application in all-solid-state lithium battery) and/or the particle coatings to minimize the copper migration in such cells.

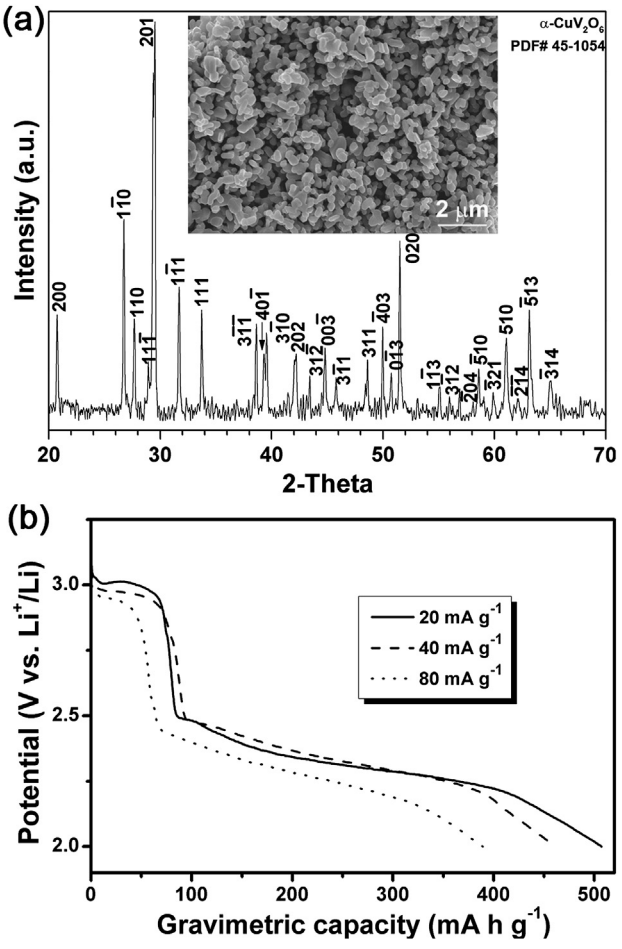

Fig. 4. (a) XRD profile of α-CuV_2O_6 synthesized by heat treatment of ε-$Cu_{0.95}V_2O_5$ superstructures at 500 °C in air over 4 h. SEM of the particles is shown in the inset. (b) Discharge profiles of cells made of the as-prepared α-CuV_2O_6 nanograins at various current densities of 20–80 mA g^{-1} to the cutoff voltage of 2.0 V.

Calcination in air at 500 °C for4 h is performed on the as-synthesized ε-$Cu_{0.95}V_2O_5$ hollow microspheres. All recorded X-ray reflections can be indexed according to α-CuV_2O_6 reported structure (Fig. 4a). The SEM micrograph shown in the inset depicts that the α-CuV_2O_6 nanograins are slightly agglomerated, with the lateral length and height are 120–210 and 85–350 nm, respectively. Furthermore, the calcined α-CuV_2O_6 single-crystal formation provides another piece of evidences that the aforementioned hydrothermal precipitate is pure ε-$Cu_{0.95}V_2O_5$.

Fig. 4b shows the initial discharge curves of electrodes with α-CuV_2O_6 nanograins at various current densities. At 20 mA g^{-1}, the specific discharge capacity is as high as 507 mAh g^{-1} (~$Li_{5.0}CuV_2O_6$), which is much higher than that of bulkCuV_2O_6 (326 mAh g^{-1}) and comparable to that (514 mAh g^{-1}) reported by Chen's group [27]. At higher current density of 80 mA g^{-1}, the electrode of α-CuV_2O_6 nanograins retains high capacity of 390 mAh g^{-1}, which is even 40 mAh g^{-1} higher than that of the electrode with α-CuV_2O_6 nanowires.

4. Conclusions

In summary, self-assembled ε-$Cu_{0.95}V_2O_5$ hollow microspheres from nanoribbons have been successfully synthesized by a simple, fast, and low-cost one-pot solution method. The applied fabrication methodology, that is, direct redox then combination reaction between metal-ion precursors, provides an alternative approach to ternary nanomaterials containing two elements both with versatile valences. When employed as cathode material in LIB, the prepared ε-copper vanadium bronze exhibits high electroactivity and remarkable reversibility. Combination of two redox processes (copper and vanadium) boosts a large specific capacity of 304 mAh g^{-1} (2.75 e^- per formula unit). However, its discharge capacities fade on cycling because the superstructure collapse fails to immobilize copper. To tackle this vital issue for cells operating on Li-driven Cu extrusion–insertion process, we can borrow ideas from Li-S batteries about rational electrode configuration design. Furthermore, as anticipated, single-crystalline α-CuV_2O_6 nanograins are obtained by heat treatment of the as-prepared ε-$Cu_{0.95}V_2O_5$ sample. Particularly the calcined α-CuV_2O_6 shows fascinating discharge capacity and high-rate capability, revealing its potential application in long-term and high-rate lithium primary batteries.

Acknowledgments

This work is supported by National Nature Science Foundations of China (Grant Nos. 51202242 and 21073179) and the Foundation for Innovative Research Groups of the National Natural Science Foundation of China (20921002).

Appendix A. Supplementary material

Supplementary material associated with this article can be found, in the online version, at http://dx.doi.org/10.1016/j.jpowsour.2013.03.002.

References

[1] P. Poizot, S. Laruelle, S. Grugeon, L. Dupont, J.M. Tarascon, Nature 407 (2000) 496–499.
[2] Y. Liu, Y. Takeda, T. Matsumura, J. Yang, N. Imanishi, A. Hirano, O. Yamamoto, J. Electrochem. Soc. 153 (2006) A437–A444.
[3] H. Li, G. Richter, J. Maier, Adv. Mater. 15 (2002) 736–739.
[4] S.H. Ng, N.T. Kirill, G. Bramnik, H. Hibst, P. Novak, Chem. Eur. J. 14 (2008) 11141–11148.
[5] V. Bodenez, L. Dupont, M. Morcrette, C. Surcin, D.W. Murphy, J.M. Tarascon, Chem. Mater. 18 (2006) 4278–4287.
[6] R. Schollhorn, Chem. Mater. 8 (1996) 1747–1757.

[7] M. Morcrette, P. Rozier, L. Dupont, E. Mugnier, L. Sannier, J. Galy, J.M. Tarascon, Nat. Mater. 2 (2003) 755–761.
[8] C.K. Chan, H. Peng, G. Liu, K. McIlwrath, X.F. Zhang, R.A. Huggins, Y. Cui, Nat. Nanotechnol. 3 (2008) 31–35.
[9] P.G. Bruce, S.A. Freunberger, L.J. Hardwick, J.M. Tarascon, Nat. Mater. 11 (2012) 19–29.
[10] P.G. Bruce, B. Scrosati, J.M. Tarascon, Angew. Chem. Int. Ed. 47 (2008) 2930–2946.
[11] Y. Wang, G.Z. Cao, Adv. Mater. 20 (2008) 2251–2269.
[12] Y.G. Guo, J.S. Hu, L.J. Wan, Adv. Mater. 20 (2008) 2878–2887.
[13] G. Sperlich, W.D. Laze, G. Bang, Solid State Commun. 16 (1975) 489–492.
[14] F.G. Alvarado, J.M. Tarascon, B. Wilkens, J. Electrochem. Soc. 139 (1992) 3206–3214.
[15] M. Kamata, G. Oriji, Y. Katamaya, T. Miura, T. Kishi, Solid State Ionics 146 (2002) 95–100.
[16] F.G. Alvarado, J.M. Tarascon, Solid State Ionics 63–65 (1993) 401–406.
[17] P. Rozier, M. Dolle, J. Galy, J. Solid State Chem. 182 (2009) 1481–1491.
[18] C.K. Chan, H. Peng, R.D. Twesten, K. Jarausch, X.F. Zhang, Y. Cui, Nano Lett. 7 (2007) 490–495.
[19] Z.L. Wang, D. Xu, L.M. Wang, X.B. Zhang, ChemPlusChem 77 (2012) 124–128.
[20] F. Sauvage, V. Bodenez, J.M. Tarascon, K.R. Poeppelmeier, J. Am. Chem. Soc. 132 (2010) 6778–6782.
[21] C.J. Patridge, C. Jaye, H.S. Zhang, A.C. Marschilok, D.A. Fischer, E.S. Takeuchi, S. Banerjee, Inorg. Chem. 48 (2009) 3145–3152.
[22] W. Hu, X.B. Zhang, Y.L. Cheng, Y.M. Wu, L.M. Wang, Chem. Commun. 47 (2011) 5250–5252.
[23] C.R. Xiong, A.E. Aliev, B. Gnade, K.J. Balkus, ACS Nano 2 (2008) 293–301.
[24] W. Hu, X.B. Zhang, Y.L. Cheng, C.Y. Wu, F. Cao, L.M. Wang, ChemSusChem 4 (2011) 1091–1094.
[25] L.F. Bai, J.B. Zhu, X.D. Zhang, Y. Xie, J. Mater. Chem. 22 (2012) 16957–16963.
[26] E.M. Sorensen, H.K. Izumi, J.T. Vaughey, C.L. Stern, K.R. Poeppelmeier, J. Am. Chem. Soc. 127 (2005) 6347–6352.
[27] H. Ma, S.Y. Zhang, W.Q. Ji, Z.L. Tao, J. Chen, J. Am. Chem. Soc. 130 (2008) 5361–5367.
[28] L. Zhou, W.J. Cui, J.M. Wu, Q.F. Zhao, H.X. Li, Y.Y. Xia, Y.H. Wang, C.Z. Yu, Nanoscale 3 (2011) 999–1003.
[29] J.I. Yamaura, M. Isobe, H. Yamada, T. Yamauchi, Y. Ueda, J. Phys. Chem. Solids 63 (2002) 957–960.
[30] W.S. Hulscher, G.H. Jonker, J. Am. Ceram. Soc. 55 (1972) 632–634.
[31] O. Mentre, M. Huve, F. Abraham, J. Solid State Chem. 145 (1999) 186–196.
[32] J.M. Savariault, E. Deramond, J. Galy, Z. Kristallogr. 209 (1994) 405–412.
[33] J.H. Huang, L.A. Gao, Cryst. Growth Des. 6 (2006) 1528–1532.
[34] S.D. Zhang, Y.M. Li, C.Z. Wu, F. Zheng, Y. Xie, J. Phys. Chem. C 113 (2009) 15058–15067.
[35] C. Delmas, H. Cognac-Auradou, J.M. Cocciantelli, M. Menetrier, J.P. Doumerc, Solid State Ionics 69 (1994) 257–264.
[36] J. Kawakita, H. Sasaki, M. Eguchi, T. Miura, T. Kish, J. Power Sources 70 (1998) 28–33.
[37] S.S. Marcos, P.L. Moises, R.G. Benito, S. Veronica, A.C.D. Miguel, Angew. Chem. Int. Ed. 51 (2012) 3877–3882.
[38] D.Y. Chen, X. Mei, G. Ji, M.H. Lu, J.P. Xie, J.M. Lu, J.Y. Lee, Angew. Chem. Int. Ed. 51 (2012) 2409–2413.
[39] A.M. Cao, J.S. Hu, H.P. Liang, L.J. Wan, Angew. Chem. Int. Ed. 44 (2005) 4391–4395.